Methods

Retinal Ganglion Cell Degeneration in a Rat Magnetic Bead Model of Ocular Hypertensive Glaucoma

James R. Tribble[1], Amin Otmani[1], Eirini Kokkali[2], Emma Lardner[1], James E. Morgan[2,3], and Pete A. Williams[1]

[1] Department of Clinical Neuroscience, Division of Eye and Vision, St. Erik Eye Hospital, Karolinska Institutet, Stockholm, Sweden
[2] School of Optometry and Vision Sciences, Cardiff University, Cardiff, Wales, UK
[3] School of Medicine, Cardiff University, Cardiff, Wales, UK

Correspondence: Pete A. Williams, Department of Clinical Neuroscience, Division of Eye and Vision, St. Erik Eye Hospital, Karolinska Institutet, Stockholm 171 77, Sweden. e-mail: pete.williams@ki.se

Purpose: Glaucoma remains a leading cause of irreversible blindness worldwide. Animal glaucoma models replicate high intraocular pressure, a risk factor for glaucoma, to induce retinal ganglion cell (RGC) degeneration. We describe an inducible, magnetic bead model in the Brown Norway rat in which we are able to determine degeneration across multiple RGC compartments at a time point that is appropriate for investigating neurodegenerative events and potential treatment effects.

Methods: We induced ocular hypertension through injection of magnetic microspheres into the anterior chamber of Brown Norway rats; un-operated (naïve) rats served as controls. Intraocular pressure was recorded, and eye diameter measurements were taken before surgery and at the terminal end points. We assessed RGC degeneration and vascular changes through immunofluorescence, and axon transport to terminal brain thalami through intravitreal injection of fluorophore-conjugated cholera toxin subunit β.

Results: We observed clinically relevant features of disease accompanying RGC cell somal, axonal, and dendritic loss. RGC axonal dysfunction persisted along the trajectory of the cell into the terminal brain thalami, with clear disruption at the optic nerve head. We also observed vascular compromise consistent with human disease, as well as an expansion of global eye size with ocular hypertension.

Conclusions: The magnetic bead model in the Brown Norway rat recapitulates many clinically relevant disease features of human glaucoma, including degeneration across multiple RGC compartments. Eye expansion is likely a result of rodent scleral elasticity, and we caution that this should be considered when assessing retinal density measurements.

Translational Relevance: This model offers a disease-relevant platform that will allow for assessment of glaucoma-relevant therapeutics.

Introduction

Glaucoma is the leading cause of irreversible blindness, affecting ∼80 million people worldwide.[1] The underlying pathology is complex and characterized by the progressive dysfunction and loss of retinal ganglion cells (RGCs) and their axons. Major risk factors are increasing age, elevated intraocular pressure (IOP), and genetic predisposition. RGC degeneration is described as a compartmentalized process, where somal, axonal, and dendritic atrophy and loss differ temporally based on the insult context.[2–4] RGC soma, axon, and dendrite loss is a feature of human glaucoma[5–7] that is replicated across different animal models in multiple species.[3,8,9] Dendritic atrophy in the inner plexiform layer is well established as a sensitive marker of early degeneration, as it can be substantial even with mild RGC loss.[10–13]

Glaucoma-like insults are commonly modeled in animals by elevating IOP to ocular hypertensive levels that are induced either genetically or surgically.[14,15]

Inducible models benefit from the control of age as a risk factor and typically allow for rapid experimental time scales. A common approach is to inject microparticles into the anterior chamber which occlude the trabecular meshwork, blocking aqueous humor outflow and subsequently elevating IOP. Many variations on this method have been described.[16–18] To our knowledge, we were the first to propose the use of paramagnetic microparticles that could be directed with a magnet to the iridocorneal angle, allowing for control of distribution and avoidance of disruption to vision through occlusion of the pupil.[19] We have since used this model to investigate RGC dendritic atrophy,[20,21] and others have adapted its use for mice,[22,23] but a detailed characterization of the rat model has yet to be performed. We use the Brown Norway rat (*Rattus norvegicus*) because (1) it is the rat genetic standard (and as such will allow for detailed -omics analysis (e.g., KEGG pathways based on Brown Norway gene annotations); (2) their temperament is amenable to ophthalmic examination without the need for restraint or anesthesia, particularly with regard to recording reliable tonometry measurements; and (3) they are pigmented and as such avoid potential confounders present in albino rodents (e.g., Wistar and Sprague–Dawley rats), which have reduced ipsilateral projections.[24–27] We describe an updated method for bead preparation and injection and assess degeneration across multiple RGC compartments in this model. Its ease of use, high replicability, and similarities to human glaucomatous disease should facilitate the use of this model for disease and treatment discovery and testing.

Methods

Rat Strain and Husbandry

Adult, male Brown Norway rats (12–16 weeks old, weighing 300–375 g; SCANBUR, Karlslunde, Denmark) were housed and fed in a 12-hour light/dark cycle with food and water available ad libitum. All experimental procedures were undertaken in accordance with the ARVO Statement for the Use of Animals in Ophthalmic and Research. Individual study protocols were approved by Stockholm's Committee for Ethical Animal Research (10389-2018). All data generated or analyzed during this study are included in this published article.

Induction of Ocular Hypertension

Ocular hypertension (OHT) was induced bilaterally (*n* = 23 rats, 46 eyes). Normotensive (NT) eyes in bilateral un-operated (naïve) rats served as controls (*n* = 19 rats, 38 eyes). OHT was induced using a magnetic microbead injection model[14,19] with modifications detailed below and in Table 1. Microbeads (4.5-μm diameter; Dynabeads M-450 Epoxy; Thermo Fisher Scientific, Waltham, MA) were prepared for injection by washing with $1\times$ Hanks' Balanced Salt Solution (HBSS, no calcium, no magnesium, no phenol red; Thermo Fisher Scientific) and resuspended in a $0.25\times$ volume of HBSS ($\sim 1.6 \times 10^6$ beads/μL). These beads were selected due to their hydrophobic nature, which allows for easy dispersion within the anterior chamber, and the surface epoxy groups bind amino and hydroxyl groups (present on many cell surfaces), which may account for their observed retention within the iridocorneal angle. Previous use of uncoated beads had required repeat injections, as beads were often not retained in the iridocorneal angle over time (Table 1). Rats were anesthetized with an intraperitoneal injection of ketamine (37.5 mg/kg) and medetomidine hydrochloride (1.25 mg/kg). Using a NanoFil syringe (World Precision Instruments, Sarasota, FL) with a 33-gauge tribeveled needle, 6 to 8 μL of bead solution was injected into the anterior chamber of the eye using a tunnel incision through the cornea. Beads were distributed to block the iridocorneal angle using a handheld rare earth magnet (cylindrical with a 4-mm diameter).

IOP was measured using a TonoLab rebound tonometer (Icare, Vantaa, Finland) in awake and unrestrained rats. Rats were habituated to the tonometry procedure the week before surgery through familiarization with extended handling and tonometry training. Baseline IOP was recorded on the day of surgery (preoperatively, awake and unrestrained; day 0) and recorded every 2 to 4 days afterward until the endpoint (postoperative day 14), with IOP recordings always being taken between 9 AM and 10 AM to avoid the effects of circadian rhythm on IOP (2–3 hours from lights on). IOP was taken as the average of five tonometer readings. NT rats followed the same 14-day time course (without surgery). In a subset of animals (*n* = 6 NT eyes, *n* = 6 OHT eyes), IOP was recorded 6, 24, and 72 hours after induction of OHT. IOP was expressed as an area under the curve (AUC) for the IOP profile, a mean across all days, and the peak of IOP identified (analyzed by a Kruskal–Wallis test followed by Dunn's test with Benjamini and Hochberg correction).

General Histopathology

Rats were heavily anesthetized at day 14 by intraperitoneal injection of pentobarbital (75 mg/kg) and euthanized by cervical dislocation. Eyes were

Table 1. Bead Protocol Changes

Protocol	Bead Details	Bead Preparation	Bead Concentration	Injection Details	Time Frame
Samsel et al.[19]	5-µm diameter ferromagnetic microspheres (Corpuscular, Inc., Cold Spring, NY)	Sterilized by gamma irradiation	30 mg/mL	10–20 µL delivered by unilateral tunnel injection	42 days, with up to 3 repeat injections
Williams et al.[20]	Dynabead M-450 Epoxy, 4.5-µm diameter (Thermo Fisher Scientific)	Washed in 1-M Tris buffer solution (pH 11) for 24 hours at 4°C, reconstituted in BSS, sterilized by gamma irradiation	30 mg/mL	10 µL delivered by unilateral tunnel injection	16 days with repeat injections, if necessary
Tribble et al.[21]	4.5-µm diameter paramagnetic polystyrene microspheres (Kisker Biotech, Steinfurt, Germany)	4× centrifugation (1600g) and washing in BSS, sterilized by gamma irradiation	30 mg/mL (4.7 × 10^5 beads)	10 µL delivered by unilateral tunnel injection	20 days of OHT (followed by 14 days of return to NT); repeat injections undertaken, if necessary, with 1 week interval
This study	Dynabead M-450 Epoxy, 4.5-µm diameter (Thermo Fisher Scientific)	2× centrifugation (1000g) and washing in HBSS	~1.6 × 10^6 beads/µL	6–8 µL delivered per eye by bilateral tunnel injection; no repeat injections	14 days OHT

immediately enucleated (with 1 mm of optic nerve post-globe preserved) and immersed in 3.7% paraformaldehyde (PFA) in 1× phosphate-buffered saline (PBS). Eye orientation was maintained with a mark on the corneal surface (nasal midline scratch from a 32-gauge needle following euthanasia but prior to enucleation). Brains (with attached optic nerves) were removed and immersed in 3.7% PFA in 1× PBS. Eyes, optic nerves, and brains for cryosectioning were maintained in fixative for 24 hours before cryoprotecting in 30% sucrose in 1× PBS for 24 hours, freezing in optimal cutting temperature medium (Sakura, Alphen aan den Rijn, The Netherlands) on dry ice, and storage at –80°C. Cryosections were cut on a cryostat (CryoStar NX70; Thermo Fisher Scientific) and stored at –20°C. Eyes were sectioned at 20-µm thickness (saggital plane), with sections maintained from ~200 µm nasal to ~200 µm temporal of the optic nerve head. Optic nerves were separated at the chiasm with a diagonal cut used to maintain orientation and sectioned at

20 μm to generate transverse nerve sections. Brains were serial sectioned (coronal plane) at 50 μm from –4 mm caudal of cranial landmark Bregma to – 8 mm caudal of Bregma in order to capture the entire dorsal lateral geniculate nucleus (dLGN) and the superior colliculus (SC). Eyes for paraffin sectioning were prepared in paraffin and sectioned (saggital plane) to give optic nerve head sections (3-μm thickness) on a microtome (Microm HM 355S; Thermo Fisher Scientific). Optic nerves for paraffin sectioning were dissected free from the brain 2 mm post-optic chiasm with the orientation maintained as above and then prepared in paraffin for sectioning.

Immunohistochemistry and Immunofluorescence

The antibodies and stains used for immunofluorescence, immunohistochemistry, and histological labeling are detailed in Table 2. The same immunofluorescent labeling protocol was followed for cryosections, paraffin sections, and flat-mount retina, with exceptions noted where relevant. Tissue was isolated using a hydrophobic barrier pen (Avantor, Radnor, PA), permeabilized in 0.5% Triton X-100 in 1× PBS for 1 hour, and blocked in 5% bovine serum albumin in 1× PBS for 1 hour; primary antibody was applied overnight at 4°C (see Table 2). Tissue was then washed for 5 × 5 minutes in 1× PBS, and secondary antibody was applied (1:500 in 1× PBS) for 4 hours at room temperature, followed by washing for 5 × 5 minutes in 1× PBS. Then, 4′,6-diamidino-2-phenylindole (DAPI) nuclear stain (500 μg/mL stock; used 1:500 in 1× PBS) was applied for 10 minutes. The tissue was washed for 5 minutes in 1× PBS, dried, and mounted using Fluoromount-G and glass coverslips (Thermo Fisher Scientific). For cryosections, tissue was air dried for 15 minutes and rehydrated in 1× PBS for 15 minutes before following the protocol above. For paraffin sections, sections were deparaffinized and rehydrated through xylene and an alcohol gradient before performing antigen retrieval using ethylenediaminetetraacetic acid buffer (pH 9, 20 minutes, 100°C). Immunohistochemistry was performed in a Bond III robotic system (Leica Biosystems, Newcastle, UK).

Assessment of Neurodegeneration Following OHT

Eyes for flat-mount retina preparations were maintained in fixative as globes for 2 hours before the retina was dissected free at the optic nerve head, the vitreous removed, and the retina flat-mounted, ganglion cell layer up, on a coated glass slide (Superfrost Plus; Thermo Fisher Scientific). Retinas were labeled with antibodies against RNA-binding protein with multiple splicing (RBPMS) and isolectin B4 and were counterstained with DAPI. Flat-mounted retinas were imaged on a Zeiss Axioskop 2 Plus epifluorescence microscope (Carl Zeiss Microscopy, White Plains, NY) for quantification of RGC densities. Six images per retina (40× magnification, 0.25 μm/pixel) were taken equidistant to the optic nerve head (1000 μm eccentricity, at 12, 2, 4, 6, 8, and 10 o'clock). This method was intended to give a reproducible representation of density across retinal sectors.

Two separate experimental cohorts were evaluated. In the first, RGC loss under OHT was assessed in an experiment containing five binocular NT animals compared to five binocular OHT animals ($n = 10$ eyes per group). To assess regional loss, the six regions were divided into superior and inferior so that each region contained $n = 3$ regions of interest (ROIs). Images were cropped to 150×150 μm, and RBPMS+ cells were counted using the cell counter plugin for Fiji (ImageJ, National Institutes of Health, Bethesda, MD).[28] In the second evaluation, RGC loss at an earlier 3-day time point (where IOP was highest) was assessed in a separate cohort that included three binocular NT animals ($n = 6$ eyes); three binocular OHT animals, which were euthanized at 14 days after OHT induction ($n = 6$ eyes); and four binocular OHT animals, which were euthanized at 3 days after OHT induction ($n = 8$ eyes). Cell counts were averaged across all six images to give a retinal average and expressed as a density per 0.01 mm^2 (analyzed by one-way analysis of variance [ANOVA] with Tukey's honestly significant difference [HSD]). For flat-mount image analysis, ROIs were analyzed in a single batch with ROIs identified by an ROI number and a numeric rat ID. On cryosections ($n = 4$ NT eyes, $n = 4$ OHT eyes), neurofilament labeling at the optic nerve head was imaged by epifluorescence microscopy (as above). On paraffin sections ($n = 6$ NT eyes, $n = 10$ OHT eyes), hematoxylin and eosin (H&E) and Nissl staining were performed and imaged on an Olympus IX73 inverted microscope (20×, tiled color image, 0.51 μm/pixel; Olympus, Tokyo, Japan).

The optic nerve head was qualitatively assessed as either normal or cupped. Optic nerve axon loss was assessed in 3-μm transverse paraffin sections ($n = 4$ NT nerves, $n = 5$ OHT nerves). Sections were labeled with antibodies targeting neurofilament M (NF-M) and myelin basic protein (MBP), and images were acquired on a Zeiss LSM 800 with Airyscan (63× and 1.3× optical zoom, 35 nm/pixel). Five 66.76 ×

translational vision science & technology

Table 2. Antibody Details

Antibody	Target	Host	Dilution	Manufacturer (Catalog No.)	Use
βIII-tubulin	Microtubules specific to RGCs	Chicken	1:250	Novus Biologicals (NB100-1612)	IF[a]
Isolectin GS-IB$_4$ (IsoB4)	Poly-N-acetyllactosamine, found on microglia, endothelial cells, monocytes/macrophages	Lectin from *Griffonia simplicifolia* conjugated to biotin	0.1 mg/mL	Invitrogen (I21414)	IF[a]
NF-M	Neurofilament medium chain	Chicken	1:500	Novus Biologicals (NB300-222)	IF[a]
MBP	Myelin basic protein	Rabbit	1:4000	Abcam (ab210811)	IF[a]
MAP2	Neuronal dendrites	Chicken	1:250	Novus Biologicals (NB300-213)	IF[a]
RBPMS	RNA-binding protein, RGC specific in the retina	Rabbit	1:500	Novus Biologicals (NBP2-20112)	IF[a], IHC[b]
GFAP	Glial fibrillary acidic protein	Rabbit	1:1000	Abcam (ab207165)	IF[a]
Goat-Anti Rabbit Alexa Fluor 488	Rabbit primary antibody	Goat	1:500	Abcam (A11008)	IF[a]
Goat-Anti Rabbit Alexa Fluor 568	Rabbit primary antibody	Goat	1:500	Abcam (A11011)	IF[a]
Goat-Anti Chicken Alexa Fluor 488	Chick primary antibody	Goat	1:500	Abcam (A11039)	IF[a]
Goat-Anti Chicken Alexa Fluor 568	Chick primary antibody	Goat	1:500	Abcam (A11041)	IF[a]
Streptavidin Alexa Fluor 488 conjugate	Biotin	Not available	4 µg/mL	Invitrogen (S11223)	IF[a]

[a]Immunofluorescence.
[b]Immunohistochemistry.

66.76-μm images were collected per nerve (size determined as the optimal for resolution using this system). NF-M-positive puncta were counted using the ImageJ cell counter plugin (in Fiji) and averaged. Overview images (10×) were acquired, and the optic nerve areas from the dura mata and pia mata were calculated by tracing their outline using the polygon tool in Fiji. The average NF-M count was scaled to total optic nerve area (analyzed by unpaired, one-tailed Student's *t*-test followed by the Shapiro–Wilk test for normality).

Dendrite loss was quantified by microtubule-associated protein 2 (MAP2) staining on retinal sections ($n = 6$ NT eyes, $n = 6$ OHT eyes), and images at 1000-μm eccentricity from the optic nerve head were acquired on a Zeiss LSM 800 with Airyscan (20× optical zoom, 319.45×319.45 μm area, 0.312 μm/pixel, *z*-stack). Image parameters were kept constant. The inner plexiform layer was cropped, and the MAP2 signal was reconstructed using the Imaris 9.3.1 surfaces tool (Bitplane, Zürich, Switzerland) with thresholding to a constant range. MAP2 volume was corrected to the total cropped volume. Glial fibrillary acidic protein (GFAP) staining was assessed in optic nerve (transverse paraffin sections; $n = 4$ NT nerves, $n = 5$ OHT nerves). GFAP labeling was imaged on a Zeiss LSM 800 with Airyscan (63× and 1.3× optical zoom, 35 nm/pixel). GFAP fiber alignment (to detect process remodeling typical of gliosis in the optic nerve) was measured using OrientationJ[29] (analyzed by unpaired, one-tailed Student's *t*-test followed by Shapiro–Wilk test for normality with a squared transformation applied).

Vasculature Analysis

For retinal blood vessel analysis ($n = 10$ NT eyes, $n = 8$ OHT eyes), images were captured on a Zeiss Axioskop 2 Plus epifluorescence microscope (5× magnification, 2861.86×2144.33 μm area, 2.05 μm/pixel). Images were stitched in Fiji using the pairwise stitching plugin.[30] The isolectin B4/blood vessel channel was isolated from the image in Fiji, and the background of the image was removed by thresholding. Retinas were cropped to 3000 μm^2 to maintain consistency (representing >80% of retinal explant area). AngioTool[31] was used to measure blood vessel morphologies, including total blood vessel length, junction density, and lacunarity (a measure of space filling within the image, where a high lacunarity equals less space filling by blood vessels), with the following parameters: blood vessel diameter (8–30 μm) and pixel intensity (0–255), all analyzed by Student's *t*-test

(unpaired, two-tailed), followed by the Shapiro–Wilk test for normality.

Retinal Stretch

Ocular globe measurements were recorded using Avantor digital calipers (resolution, 0.01 mm). Eye diameter at the limbus was measured before anterior chamber bead injections in anesthetized animals ($n = 20$ OHT eyes; i.e., preoperative NT) and following enucleation after euthanasia ($n = 31$ NT eyes, $n = 35$ OHT eyes). Axial length (diameter from cornea to optic nerve) was also measured post-enucleation ($n = 31$ NT eyes, $n = 35$ OHT eyes). To determine whether retinal stretch also occurred in OHT, eyes were processed for paraffin sectioning as above ($n = 6$ NT eyes, $n = 8$ OHT eyes). All eyes were treated as a single batch (length of fixation, paraffin embedding), and all paraffin sections were dehydrated and stained as a single batch to prevent batch effects. Sections through the optic nerve head (3-μm thickness) were labeled for RBPMS in a BOND III robotic system using BOND Polymer Refine Red Detection (Leica Biosystems) and imaged on an Olympus IX73 inverted microscope (20×, tiled color image, 0.51 μm/pixel). Retinal length was measured in Fiji by tracing along the lower boundary of the outer nuclear layer (because this layer retains a straight boundary free from OHT-induced changes). RBPMS counts across the whole retina were performed using the cell counter plugin and expressed as a density. Spearman's correlations were performed in R (R Foundation for Statistical Computing, Vienna, Austria) for comparisons of eye size, IOP measures, RBPMS density, retinal length, and animal weight. RBPMS density and retinal length were also compared between NT and OHT eyes by Student's *t*-test (unpaired, two-tailed, followed by the Shapiro–Wilk test for normality).

Cholera Toxin Tracing

Intravitreal injection of cholera toxin was used as a neuronal tracer to visualize RGC projections and measure axon transport. At day 11, rats were anesthetized as above, and 3 μL of Alexa Fluor 488 (AF488) or Alexa Fluor 594 (AF594) conjugated cholera toxin, subunit β (CT-β; Thermo Fisher Scientific), was injected intravitreally using a NanoFil syringe with 33-gauge tribeveled needle. CT-β was injected rapidly, and the syringe was withdrawn after 30 seconds. CT-β AF488 was injected into the left eye and CT-β AF594 into the right eye ($n = 6$ NT eyes, $n = 6$ OHT eyes). Rats were euthanized on day 14 as above. Flat-mounted optic nerves and optic

chiasms and flat-mounted SC were imaged on a Zeiss Axioskop 2 Plus epifluorescence microscope (5× and 2.5× magnification, respectively). Eyes, optic nerves, and brains ($n = 6$ per group) were cryosectioned (20-μm thickness) and stored as above before labeling with DAPI and mounting. For optic nerves, proximal sections were cut ∼2 mm posterior to the eye globe, and distal sections were cut ∼2 mm from the chiasm. CT-β labeling at the optic nerve head was imaged on a Zeiss LSM 800 with Airyscan (10×, 0.62 μm/pixel). Stalling of axon transport at the level of the optic nerve head was qualitatively assessed.

Axon transport through the optic nerve to the terminal thalami was assessed quantitatively. Transverse optic nerve sections and coronal brain sections were imaged on a Zeiss Axioskop 2 Plus epifluorescence microscope (optic nerves, 10×, 1.03 μm/pixel; dLGN, 5×, 2.05 μm/pixel; SC, 2.5×, 4.25 μm/pixel). CT-β labeling was quantified within the optic nerve (proximal and distal), dLGN, and SC in Fiji ($n = 6$ optic nerve, $n = 6$ dLGN, $n = 6$ SC per group; $n = 3$ sections analyzed and averaged for each). In whole optic nerve sections, or dLGN and SC isolated using DAPI as an anatomical guide (using the polygon tool in Fiji), the mean pixel intensity was calculated in the red and green channels (analyzed by unpaired, one-tailed Student's *t*-test followed by the Shapiro–Wilk test for normality). To assess the degree of space filling, fractal analysis was performed in Fiji (fractal box count using boxes of size 2, 3, 4, 6, 8, 12, 16, 32, and 64; analyzed by unpaired, one-tailed Student's *t*-test followed by the Shapiro–Wilk test for normality). The extent of contralateral and ipsilateral projections was estimated in the dLGN by measuring the area occupied by red or green labeling using the polygon tool in Fiji, and the values were expressed as a percentage of total area (analyzed by unpaired, one-tailed Student's *t*-test followed by the Shapiro–Wilk test for normality). Comparison of these measurements in NT and OHT tissue was used to evaluate the degree of axon transport loss.

Statistical Analysis

All statistical analysis was performed in R. Data were tested for normality with a Shapiro–Wilk test. Normally distributed data were analyzed by Student's *t*-test or ANOVA (with Tukey's HSD). Non-normally distributed data were transformed using squared transforms; data that remained non-normally distributed were analyzed by a Kruskal–Wallis test followed by Dunn's tests with Benjamini and Hochberg correction. Statistical tests are detailed at point of use. Unless otherwise stated, $^*P < 0.05$, $^{**}P < 0.01$, and $^{***}P <$ 0.001; NS, non-significant ($P > 0.05$). For box plots, the center hinge represents the mean with upper and lower hinges representing the first and third quartiles; whiskers represent 1.5 times the interquartile range.

Results

OHT in the Rat Magnetic Bead Model Demonstrates Reproducible Degeneration Across Multiple RGC Compartments

Following intracameral injection (Fig. 1A), paramagnetic beads were directed to the iridocorneal angle (Fig. 1B). Clinically relevant histopathology confirmed that beads were maintained in the angle for the duration of the experiment, with beads evident within the drainage structures of the trabecular meshwork and Schlemm's canal (Fig. 1B). This resulted in a significant and robust IOP increase that was sustained until euthanasia (Fig. 1C). Peak IOP occurred at 3 days post-induction (Fig. 1C). Fourteen days of sustained OHT resulted in cupping of the optic nerve head which was qualitatively assessed in H&E and Nissl stained sections (0/6 cupped in NT eyes, 6/8 cupped in OHT eyes) (Figs. 1D–1F). RBPMS labeling demonstrated significant loss of RGCs at 14 days post-injection, with RGC density reduced in OHT eyes compared to NT eyes (Fig. 1G). There was no RGC death detected at 3 days post-induction, which, in combination with an absence of large IOP spikes, supports a pathology without early ischemia-related RGC death. There was a small increase in the nearest neighbor distance between RGCs in OHT eyes; although this increase was small (30% increase in OHT compared to NT), the range of values for OHT was increased (doubling of the interquartile range in OHT). There was no detectable difference in RGC density between superior and inferior retina in OHT eyes. Collectively, these data suggest diffuse and random RGC death (i.e., not regional cell loss) (Fig. 1G). We have previously demonstrated RGC dendritic atrophy at the single RGC level.[20,21] Supporting this, RGC dendritic loss in the inner plexiform layer in OHT eyes was observed through a reduction in reconstructed MAP2 volume (Fig. 1H).

RGC Degenerative Processes Extend into Terminal Brain Regions

RGC neurodegeneration during glaucoma is a compartmentalized event, with OHT driving dendritic and synaptic retraction, soma degeneration, and
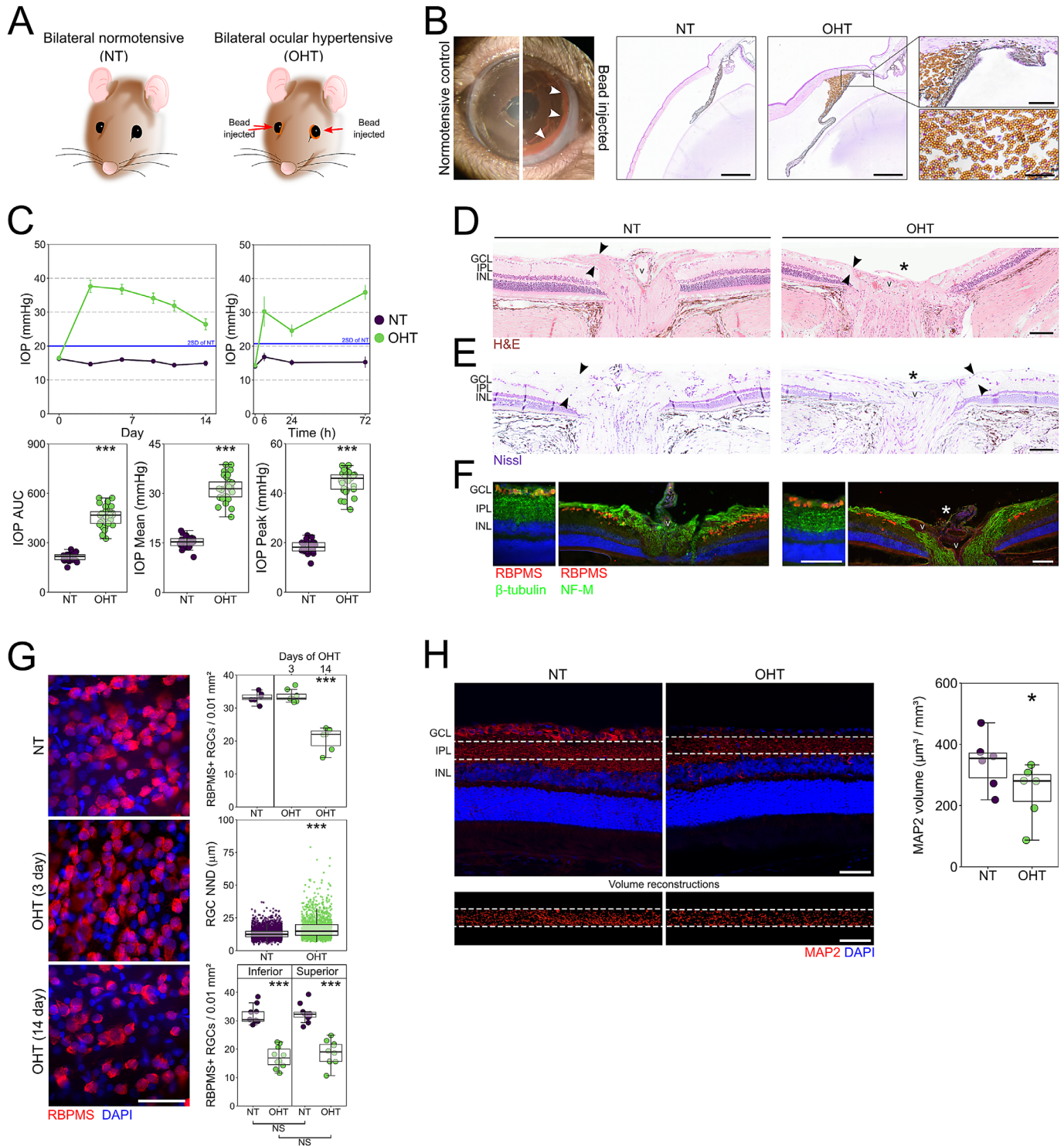
Figure 1. Induction of OHT via paramagnetic bead induction. (**A**) Brown Norway rats underwent intracameral injections of paramagnetic beads bilaterally. Naïve, un-operated animals served as controls. (**B**) Beads were directed into the drainage structures of the eye via a rare-earth magnet (5-mm tip) (*left panel*). Histology (*right panels* and *insets*) demonstrated that beads remained within the drainage structures of the trabecular meshwork and Schlemm's canal. This resulted in a significant and robust IOP increase, peaking at 72 hours post-induction and sustaining until euthanasia. *Scale bars*: 500 μm (*right panels*); 100 μm (*right inset, upper*); 50 μm (*right inset, lower*). (**C**) Following 14 days of OHT, changes to the RGC layer and nerve fiber layer thinning (*black arrows* at the optic nerve head) were apparent, with qualitatively observed optic nerve excavation (*asterisk*; $n = 13$ rats and 26 eyes for NT; $n = 15$ rats and 30 eyes for OHT). Inner retinal morphology is shown through two modalities: H&E staining (**D**) and Nissl staining (**E**). *Arrows* denote the nerve fiber layer, and *v* denotes the central retinal vessel. *Scale bar*: 100 μm. (**F**) Immunofluorescence for antibodies against RGC specific markers (RBPMS, β-tubulin, NF-M). *Scale bar*: 100 μm.

$\rightarrow$

←

(**G**) RGC populations were assessed in flat-mount retinas confirming no early change in RGC density (3 days after OHT induction) and a significant loss of RGCs and increased NND of RGCs following 14 days of OHT ($n = 6$ NT; $n = 6$ OHT at 14 days; $n = 8$ OHT at 3 days). There was no detectable region-specific loss between superior and inferior retina ($n = 10$ NT eyes; $n = 10$ OHT eyes from a separate cohort of animals). *Scale bar*: 20 μm. (**H**) OHT also resulted in significant dendritic atrophy (MAP2 labeling) as assessed by MAP2 volume reconstructions in the IPL (cropped area in *white* and corresponding reconstruction below; $n = 6$ eyes for NT; $n = 6$ eyes for OHT), which is suggestive of dendritic atrophy and retraction. *Scale bar*: 50 μm. $^*P < 0.05$, $^{**}P < 0.01$, $^{***}P < 0.001$; NS, non-significant ($P > 0.05$). NND, nearest neighbor distance; IPL, inner plexiform layer.

deafferentation.[32] We confirmed loss of RGC axons in the optic nerve by counting individual nerve fibers assessed in neurofilament-labeled sections imaged at ultra-high resolution (35 nm/pixel). The estimated total number of axons in NT optic nerves (average 125,000) reflected those reported in the literature for adult Brown Norway rats.[33] The total number of axons was significantly reduced in OHT eyes compared to NT, with no significant change in optic nerve area when measured from the dura mater or pia mater (Fig. 2A). GFAP labeling in optic nerves demonstrated astrocyte remodeling, with a significant reduction in fiber coherency following periods of OHT, supporting evidence from human glaucoma and that generated from animal models of glaucoma[34,35] (Fig. 2B). These data support a model in which there is no uncoupling of axon and soma neurodegenerative events.

We next assessed axonal transport in remaining axons across the whole RGC, including projections to the dLGN and SC (Fig. 2C). In NT animals, robust labeling was evident throughout the optic nerve (with crossover at the chiasm) and persisted to the SC and dLGN (Fig. 2D). Labeling was visibly reduced in OHT eyes in the optic nerve, further reducing pre-chiasm, with reduced penetrance to the SC indicating markedly reduced axonal transport and axon degeneration (Fig. 2D). Although sectoral regions of functional axonal transport remained, this was not uniform across optic nerves or brain regions and was further evidenced in cryosections of eyes, optic nerves, and brain regions (Fig. 2E). This observation supports an absence of consistent sectoral RGC death seen in the RGC soma counts but does not preclude some level of corresponding localized dysfunction within the retina. In OHT eyes, axonal transport was largely intact within the retina, stalling at the optic nerve head myelin transition zone. Optic nerve proximal to the optic nerve head demonstrated this lack of functional transport and sectoral dysfunction that was further reduced distally, indicating both a loss of axons (axon degeneration) and a decrease in axon transport in remaining axons. Labeling in the dLGN was significantly reduced in OHT animals, as both contralateral and ipsilateral projections were significantly reduced in OHT as a percentage of overall dLGN area (but with some persisting ipsilat-

eral projections retained). This method yielded percentages similar to the known decussation rate of RGC axons to the dLGN, as well as to previously published work using this method.[36] However, because the CT-β labeling is punctate in nature, measuring the area of labeling resulted in overlapping percentages (i.e., greater than 100% combined). Labeling in the SC was also significantly reduced in OHT (Fig. 2E).

Retinal Vascular Changes Occur in the Rat Magnetic Bead Model

We and others have previously identified vascular dysfunction in the retina and ONH as a feature of human and animal glaucoma models.[37–40] Analysis of isolectin B4-labeled vessels demonstrated a significant reduction in total vessel length and junction density and an increase in lacunarity, indicting reduced vessel coverage of the inner retina (Fig. 3).

Ocular Stretch May Confound Measurement of RGC Densities in OHT Eyes

After 14 days of OHT, we observed an increase in the size of OHT eyes and hypothesized that chronic high IOP may lead to scleral remodeling and enlargement of the eye. We therefore recorded caliper measurements of the eyes before surgery (diameter at the limbus) and after euthanasia at day 14 post-OHT induction (diameter at the limbus and axial length from cornea to optic nerve) and compared those measurements to those for NT controls. OHT eyes demonstrated a significant increase in diameter by 14 days compared to both pre-surgery size (30% increase, $P < 0.001$) and NT controls (19% increase, $P < 0.001$) (Fig. 4A). The difference in the magnitude of increase is likely due to the difference in measurement pre-surgery and post-euthanasia. This is reflected in the significant difference between pre-surgery OHT eyes and NT eyes (9% increase, $P < 0.001$) (Fig. 4A). Eye diameter at the limbus and axial length at day 14 demonstrated reasonable correlation to measures of IOP, indicating a relationship between the magnitude of increase in IOP and the magnitude of increase in eye
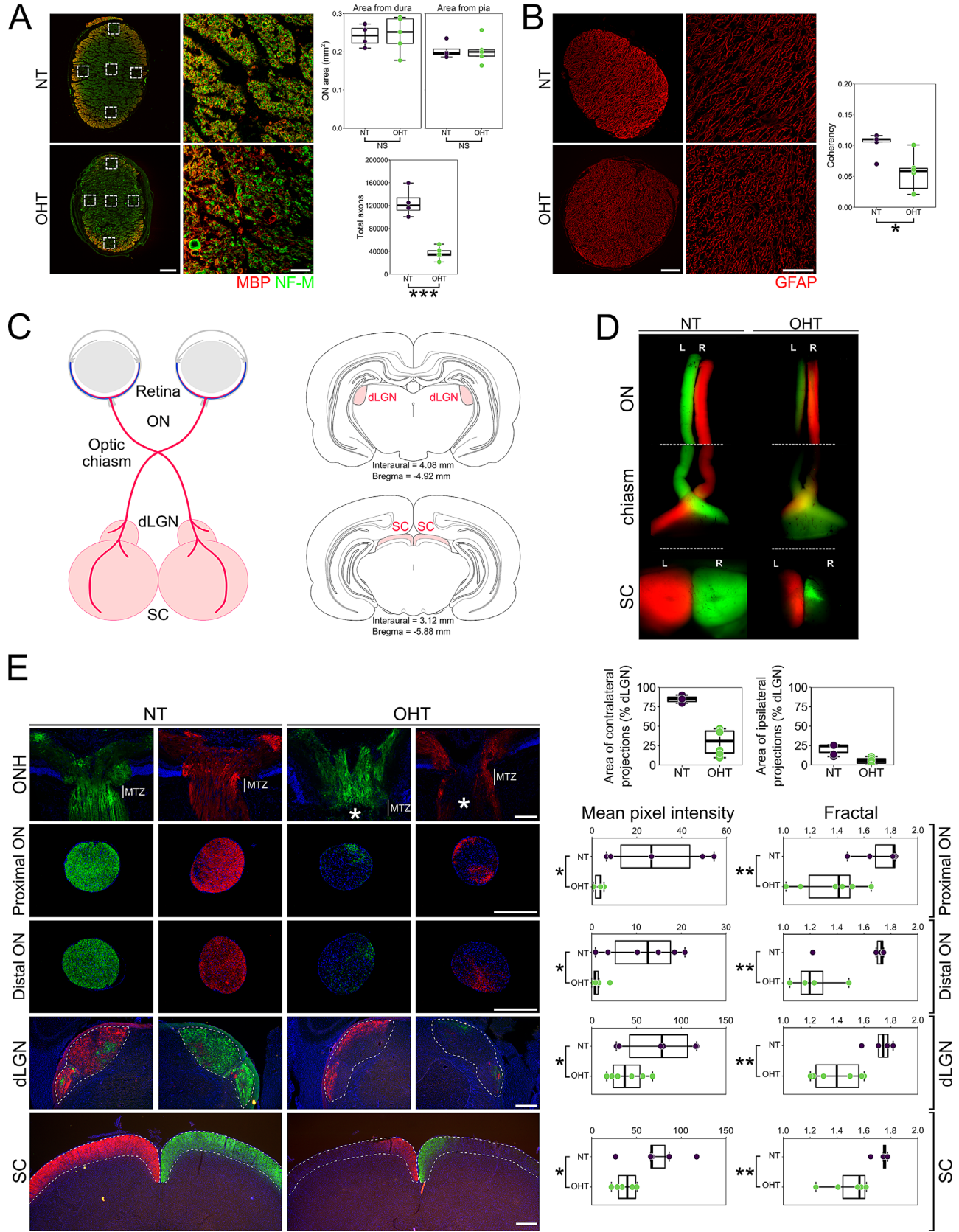
Figure 2. OHT results in axon degeneration and deficits in axoplasmic transport. (**A**) Total axon number was assessed in optic nerve sections by high-resolution imaging of NF-M-positive axon fibers and myelin bundles ($n = 4$ NT nerves; $n = 5$ OHT nerves). The estimated total number

→

←

of axons in NT optic nerves (average, 125,000) matched that reported in the literature for adult Brown Norway rats[33] and was significantly reduced in OHT eyes. The reduction is likely an overestimate due to an increased number of dystrophic axons in OHT optic nerves that may mask individual small caliber axons. There were no gross changes to optic nerve total size (as measured from the dura or pia mater), but there was a significant loss of RGC axons. *Scale bars*: 100 μm (*left panels*); 10 μm (*right insets*). (**B**) OHT results in significant remodeling of optic nerve astrocytes (a decrease in fiber alignment and coherency as assessed by OrientationJ). *Scale bars*: 100 μm (*left panels*); 50 μm (*right insets*). (**C**) Axoplasmic transport was assessed by two-color CT-β tracing from the retina to the terminal visual thalami (dLGN and SC; $n = 3$ bilateral NT animals; $n = 3$ bilateral OHT animals). A schematic showing RGC trajectories and visual thalami is shown. OHT results in an absence of axoplasmic transport to terminal regions assessed by both low-power flat-mount SCs (**D**) and in cryosections (**E**), based on mean pixel intensity and fractal analysis (for both NT and OHT, $n = 6$ eyes, $n = 6$ optic nerves, $n = 6$ dLGN hemispheres, $n = 6$ SC hemispheres). *Scale bars*: 100 μm (ONH); 500 μm (ON, dLGN, SC). Axoplasmic transport was primarily stalled within the optic nerve head (asterisk in E; at the site of the myelin transition zone [MTZ]), resulting in partial transport through the optic nerve to the dLGN and SC. Optic nerves were assessed both proximal to the eye and proximal to the chiasm. The dLGN and SC were assessed in three sections representing rostral, medial, and caudal dLGN or SC, respectively (and expressed as a mean). Both contralateral and ipsilateral projections were reduced in the dLGN (as a percentage of total dLGN area), indicating axonal transport disruption to both hemispheres from a single OHT eye. All panels in a single column (i.e., NT or OHT) are from the same visual tract. $^{*}P < 0.05$, $^{**}P < 0.01$, $^{***}P < 0.001$; NS, non-significant ($P > 0.05$). ON, optic nerve; ONH, optic nerve head.

size (Figs. 4B, 4C). There was no correlation between eye size and animal weight, confirming that neither animal age nor size was driving the observed difference (Fig. 4D).

We reasoned that an increase in eye size may cause the retina to stretch, and, as such, measurements of RGC density could be confounded, thus overestimating cell loss. Retinal length was variable in both NT eyes (8.5 ± 0.8 mm) and OHT eyes (9.5 ± 1.0 mm), and no significant increase in retinal length was observed. RGC density (as an average across the whole retina) was significantly reduced in OHT eyes compared to NT eyes (57% decrease, $P < 0.001$) (Fig. 4E). RGC density was highly correlated with IOP measures and eye size (Fig. 4F), whereas retinal length demonstrated more modest correlations (Fig. 4G). We cannot preclude changes to the tissue that may have resulted from the processing procedures, but, because all eyes were subject to the same protocol and processed as a single batch, comparisons relative to one another may diminish any possible impact of this. There is, however, no definitive way to establish the impact of a tissue processing artifact. Overall, these data demonstrate that globe expansion is a feature of the rat magnetic bead model. Although globe expansion did not result in significant retinal stretch in this dataset, analysis of the whole retinal area in flat-mount preparations may give a better indication of any possible retinal expansion that should be considered for RGC density measurements (especially reported as percentage reduction relative to the contralateral eye). Care must be used to excise the retina fully from the eye cup without leaving peripheral retina if flat-mounting tissue is to be used for measurements. These changes in size may primarily reflect expansion of the cornea as the result of anterior chamber deepening with OHT. The observed decrease in blood vessel branch-

ing density and increase in lacunarity could also be explained by the changes to globe and retina size.

Discussion

In this study, we defined the neurodegenerative components of an inducible OHT model of glaucoma. Induction of OHT by blocking aqueous humor outflow with beads has previously been achieved in a number of species.[16,18,41] Use of paramagnetic beads allows for control of distribution within the eye; it was initially described by our group[19] but with limited characterization beyond cell death in the ganglion cell layer and RGC dendritic atrophy.[20,21] Here, we have demonstrated that this model produces robust RGC soma and axon loss, axon transport dysfunction, and vascular disruption, and we confirmed the presence of dendritic atrophy.

This model demonstrated robust RGC soma and axon loss in response to sustained OHT below ischemic thresholds.[42] We saw no loss of retinal ganglion cells following 3 days of OHT, representing peak IOP in this model. Retinal ischemia induced by short-term, acute IOP elevation is frequently used to model glaucoma-like insults to the retina and optic nerve. In these models, pressure is often raised in excess of 100 mm Hg, resulting in ischemia, subsequent hypoxia, and rapid cell loss (with the range of hours to days).[43–45] We observed no ischemic IOP spike within the first 24 hours after surgery. Supporting this, short-term increases in pressures (up to 50 mm Hg) have not been found to result in ischemia or RGC loss.[46] This does not fully preclude the occurrence of an ischemic-like insult driven by hypoxia or hypoxic molecular events, but analysis of this is beyond the scope of
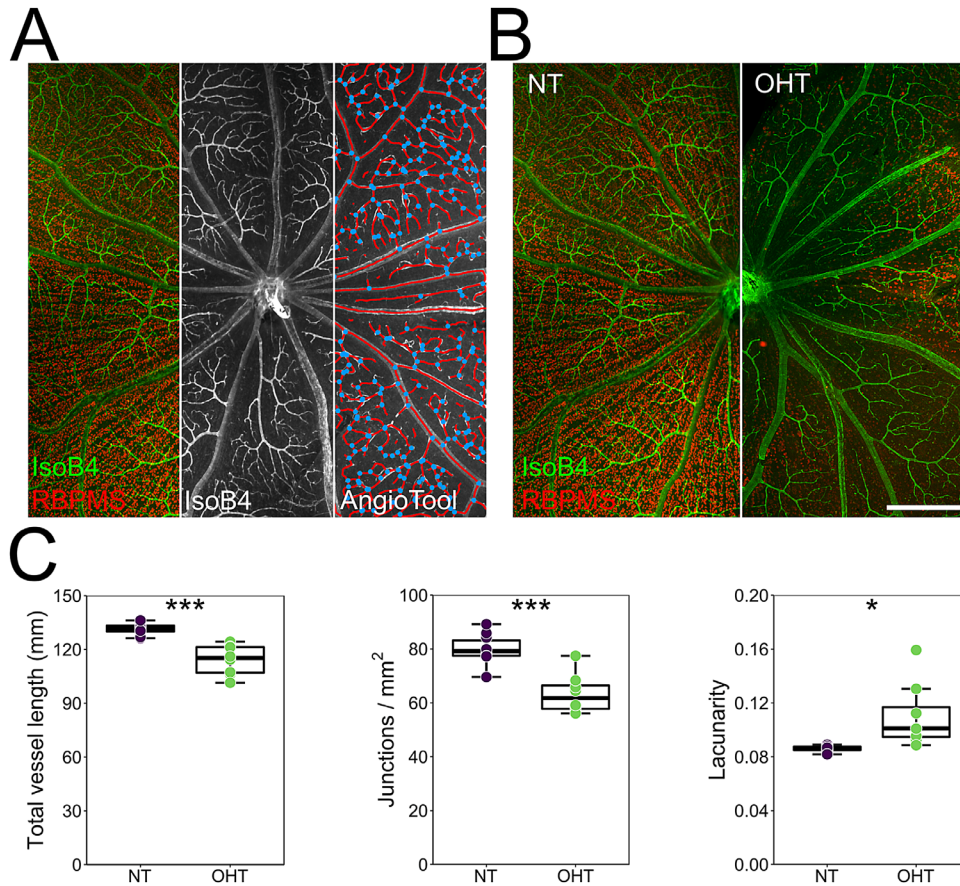
Figure 3. Vascular remodeling following OHT. (**A**) Flat-mounted retinas were labeled with isolectin B4, and the inner retina was imaged to assess blood vessel morphology ($n = 10$ NT eyes; $n = 8$ OHT eyes). Blood vessels were reconstructed with AngioTool (*right panel*; *red*, vessels; *blue*, junctions). (**B**, **C**) Following OHT there was significant vascular remodeling, as indicated by a decrease in total vessel length and number of vessel junctions and an increase in lacunarity, suggesting reduced vessel coverage of the inner retina. Lacunarity is a measure of space filling within the image, where high lacunarity equals less space filling by blood vessels. *Scale bar*: 500 μm in B. *P < 0.05, **P < 0.01, ***P < 0.001; NS, non-significant (P > 0.05).

this study. Using a rat laser photocoagulation model of OHT, Chidlow et al.[47] reported a highly variable degree of axon transport disruption and pimonidazole labeling that did not correspond statistically with the degree of IOP elevation. Furthermore, Jassim and Inman[23] observed no pimonidazole labeling in the retina 2 weeks after the induction of ocular hypertension in a mouse bead model of OHT; yet, cell loss was as great as 50% in some eyes. In this study, numerous pimonidazole-positive glia were detected at 4 weeks. These demonstrate that hypoxia can occur even during short-term, low-amplitude IOP increases but is unlikely to be a driver of major cell loss. Many independent groups have demonstrated significant short-term RGC degeneration (<21 days after ocular hypertension induction) using bead preparations without ischemic pressures.[22,23,48,49] The bead model in rodents can induce rapid RGC loss following moderate, sub-ischemic threshold IOP elevations

which is likely a feature of rodent OHT models and should be taken into account when comparing them to non-human primate models or human glaucoma samples.

RGC axon dysfunction has been well described,[50,51] and disruption of axoplasmic transport, in particular, has long been considered one of the earliest features of glaucoma,[52,53] but it is also disrupted by OHT in the absence of neurodegeneration with rapid recovery following pressure normalization.[54–56] We observed significant axon transport disruption with little CT-β labeling in the optic nerve or terminal brain regions. Our end-stage assessment reflects both axon transport deficit and axon loss in the optic nerve (given the significant reduction in axon counts). Axon loss in the optic nerve was substantial but is likely an overestimate due to an increased number of dystrophic axons in OHT optic nerves that may mask individual NF-M-positive puncta. Transmission electron microscopy
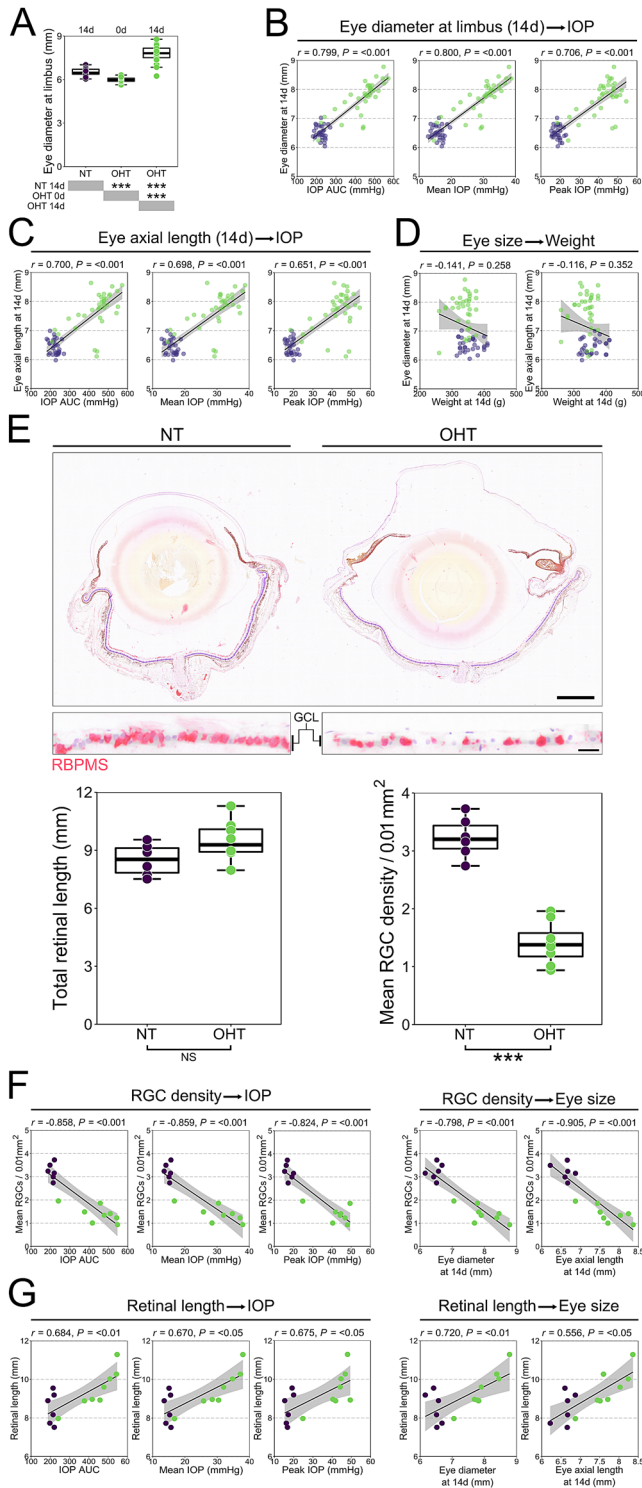
Figure 4. Sustained OHT results in ocular stretch. (**A**) OHT eyes demonstrated a significant increase in diameter by 14 days compared to both pre-surgery size and NT controls ($n = 31$ NT eyes; $n = 35$ OHT eyes, of which 20 were measured preoperatively, pre-OHT). (**B**, **C**) Eye diameter at the limbus and axial length at day 14 demonstrated reasonable correlation to measures of IOP (AUC, mean, peak), indicating a relationship between the magnitude of IOP increase and increase in the size of the eye. (**D**) These correlations were not driven by animal age or weight. (**E**) To assess retinal stretch

would be necessary to verify the true degree of axon loss and would reduce the variability in densities calculated for controls, particularly because this is the only method with sufficient resolution to identify small-caliber axons. Further experiments could explore the time course and/or reversibility of axoplasmic transport loss at different time points in this model, which could separate transport deficits from axon loss, especially as axon transport loss is an early and persistent feature of OHT rodent models, and significant failure is observed with limited axon loss.[13,50,57] Transport failure has been shown to progress in severity from distal to proximal to the retina.[50] Although minimal transport to the terminal brain regions is evident at early stages, this does not coincide with early degeneration (assessed by a global volume loss) in these regions,[50] but it is a later feature that increases with disease severity.[58] We see evidence of axoplasmic transport disruption at the level of the optic nerve head, with the majority of CT-β labeling stalling at the myelin transition zone and limited penetrance to the optic nerve and brain, as well as disruption to both contralateral and ipsilateral projections. These data corroborate clinically available human glaucoma data suggesting that damage at the site of the optic nerve head is one of the earliest key damaging events of glaucoma.[3,59]

We observed evidence of vascular compromise in the magnetic bead model. Morphological changes to vasculature have been reported in human glaucoma, including reduced arteriolar and venular vessel caliber[60,61] and reduced fractal dimension of vessel patterns.[62] It has been suggested that these changes may reflect a response to reduced metabolic demand following RGC death or that degenerative processes may impair blood vessel regulation through production of vasoconstrictive substances such as reactive oxygen species or endothelin.[37,63,64]

Following periods of OHT, we determined that global eye expansion is a feature of the paramagnetic bead model. Although this is not a feature of adult glaucoma, it occurs in congenital glaucoma, where the sclera is less rigid and more elastic.[65,66] Increased eye diameter and axial length were highly correlated with

←

following OHT, whole eyes were paraffin embedded and sectioned, and RGCs were labeled with antibodies against RBPMS ($n = 6$ NT eyes; $n = 8$ OHT eyes). There was no significant increase in total retinal length following OHT, which was highly variable even across NT eyes. RGC counts across the retina confirmed gross RGC loss. *Scale bars*: 1 mm (*upper panel*), 20 μm (*lower panel*). (**F**) RGC density was highly correlated with all measured of IOP and eye size. (**G**) Retinal length correlated with measures of IOP but to a lesser degree. For complete n values, please see the Methods section. $^*P < 0.05$, $^{**}P < 0.01$, $^{***}P < 0.001$; NS, non-significant ($P > 0.05$).

the magnitude and cumulative degree of IOP elevation. As the retina is fixed at the optic nerve and ora serrata, we reasoned that it may stretch with the eye globe. Retinal length was highly variable following OHT and trended toward an increase, but no significant change was detected. Global expansion should be considered when comparing RGC density as percentage reduction to contralateral control eyes in unilateral OHT models, particularly given that RGC numbers differ among eyes, even within individual animals where expansion may compound these errors further.[33]

Acknowledgments

References

1. Tham YC, Li X, Wong TY, Quigley HA, Aung T, Cheng CY. Global prevalence of glaucoma and projections of glaucoma burden through 2040: a systematic review and meta-analysis. *Ophthalmology*. 2014;121(11):2081–2090.

2. Buckingham BP, Inman DM, Lambert W, et al. Progressive ganglion cell degeneration precedes neuronal loss in a mouse model of glaucoma. *J Neurosci*. 2008;28(11):2735–2744.

3. Howell GR, Libby RT, Jakobs TC, et al. Axons of retinal ganglion cells are insulted in the optic nerve early in DBA/2J glaucoma. *J Cell Biol*. 2007;179(7):1523–1537.

4. Schlamp CL, Li Y, Dietz JA, Janssen KT, Nickells RW. Progressive ganglion cell loss and optic nerve degeneration in DBA/2J mice is variable and asymmetric. *BMC Neurosci*. 2006;7:66.

5. Kerrigan LA, Zack DJ, Quigley HA, Smith SD, Pease ME. TUNEL-positive ganglion cells in human primary open-angle glaucoma. *Arch Ophthalmol*. 1997;115(8):1031–1035.

6. Quigley HA, Dunkelberger GR, Green WR. Chronic human glaucoma causing selectively greater loss of large optic nerve fibers. *Ophthalmology*. 1988;95(3):357–363.

7. Tribble JR, Vasalauskaite A, Redmond T, et al. Midget retinal ganglion cell dendritic and mitochondrial degeneration is an early feature of human glaucoma. *Brain Commun*. 2019;1(1): fcz035.

8. Morrison JC, Moore CG, Deppmeier LMH, Gold BG, Meshul CK, Johnson EC. A rat model of chronic pressure-induced optic nerve damage. *Exp Eye Res*. 1997;64(1):85–96.

9. Samuels BC, Siegwart JT, Zhan W, et al. A novel tree shrew (*Tupaia belangeri*) model of glaucoma. *Invest Ophthalmol Vis Sci*. 2018;59(7):3136–3143.

10. Weber AJ, Harman CD. BDNF preserves the dendritic morphology of alpha and beta ganglion cells in the cat retina after optic nerve injury. *Invest Ophthalmol Vis Sci*. 2008;49(6):2456–2463.

11. Shou TD, Liu J, Wang W, Zhou YF, Zhao KX. Differential dendritic shrinkage of alpha and beta retinal ganglion cells in cats with chronic glaucoma. *Invest Ophthalmol Vis Sci*. 2003;44(7):3005–3010.

12. Feng L, Zhao Y, Yoshida M, et al. Sustained ocular hypertension induces dendritic degeneration of mouse retinal ganglion cells that depends on cell type and location. *Invest Ophthalmol Vis Sci*. 2013;54(2):1106–1117.

13. Risner ML, Pasini S, Cooper ML, Lambert WS, Calkins DJ. Axogenic mechanism enhances retinal ganglion cell excitability during early progression in glaucoma. *Proc Natl Acad Sci USA*. 2018;115(10):E2393–E402.

14. Morgan JE, Tribble JR. Microbead models in glaucoma. *Exp Eye Res*. 2015;141:9–14.

15. Fernandes KA, Harder JM, Williams PA, Rausch RL, Kiernan AE, Nair KS, et al. Using genetic mouse models to gain insight into glaucoma: Past results and future possibilities. *Exp Eye Res*. 2015;141:9–14.

16. Cone FE, Steinhart MR, Oglesby EN, Kalesnykas G, Pease ME, Quigley HA. The effects of anesthesia, mouse strain and age on intraocular pressure and an improved murine model of experimental glaucoma. *Exp Eye Res*. 2012;99(1):27–35.

17. Sappington RM, Carlson BJ, Crish SD, Calkins DJ. The microbead occlusion model: a paradigm for induced ocular hypertension in rats and mice. *Invest Ophthalmol Vis Sci*. 2010;51(1):207–216.

18. Frankfort BJ, Khan AK, Tse DY, et al. Elevated intraocular pressure causes inner retinal dysfunction before cell loss in a mouse model of experimental glaucoma. *Invest Ophthalmol Vis Sci*. 2013;54(1):762–770.

19. Samsel PA, Kisiswa L, Erichsen JT, Cross SD, Morgan JE. A novel method for the induction of experimental glaucoma using magnetic microspheres. *Invest Ophthalmol Vis Sci*. 2011;52(3):1671–1675.

20. Williams PA, Tribble JR, Pepper KW, et al. Inhibition of the classical pathway of the complement cascade prevents early dendritic and synaptic degeneration in glaucoma. *Mol Neurodegener*. 2016;11:26.

21. Tribble JR, Williams PA, Caterson B, Sengpiel F, Morgan JE. Digestion of the glycosaminoglycan extracellular matrix by chondroitinase ABC supports retinal ganglion cell dendritic preservation in a rodent model of experimental glaucoma. *Mol Brain*. 2018;11(1):69.

22. Ito YA, Belforte N, Cueva Vargas JL, Di Polo A. A magnetic microbead occlusion model to induce ocular hypertension-dependent glaucoma in mice. *J Vis Exp*. 2016(109):e53731.

23. Jassim AH, Inman DM. Evidence of hypoxic glial cells in a model of ocular hypertension. *Invest Ophthalmol Vis Sci*. 2019;60(1):1–15.

24. Balkema GW, Pinto LH, Dräger UC, Vanable JW. Characterization of abnormalities in the visual system of the mutant mouse pearl. *J Neurosci*. 1981;1(11):1320–1329.

25. Ahmed AK, Guison NG, Yamadori T. A retrograde fluorescent-labeling study of direct relationship between the limbic (anterodorsal and anteroventral thalamic nuclei) and the visual system in the albino rat. *Brain Res*. 1996;729(1):119–123.

26. Dreher B, Sefton AJ, Ni SY, Nisbett G. The morphology, number, distribution and central projections of Class I retinal ganglion cells in albino and hooded rats. *Brain Behav Evol*. 1985;26(1):10–48.

27. Lund RD. Uncrossed visual pathways of hooded and albino rats. *Science*. 1965;149(3691):1506–1507.

28. Schindelin J, Arganda-Carreras I, Frise E, et al. Fiji: an open-source platform for biological-image analysis. *Nat Methods*. 2012;9(7):676–682.

29. Rezakhaniha R, Agianniotis A, Schrauwen JT, et al. Experimental investigation of collagen waviness and orientation in the arterial adventitia using confocal laser scanning microscopy. *Biomech Model Mechanobiol*. 2012;11(3-4):461–473.

30. Preibisch S, Saalfeld S, Tomancak P. Globally optimal stitching of tiled 3D microscopic image acquisitions. *Bioinformatics*. 2009;25(11):1463–1465.

31. Zudaire E, Gambardella L, Kurcz C, Vermeren S. A computational tool for quantitative analysis of vascular networks. *PLoS One*. 2011;6(11):e27385.

32. Whitmore AV, Libby RT, John SWM. Glaucoma: thinking in new ways – a role for autonomous axonal self-destruction and other compartmentalised processes? *Prog Retin Eye Res*. 2005;24(6):639–662.

33. Cepurna WO, Kayton RJ, Johnson EC, Morrison JC. Age related optic nerve axonal loss in adult Brown Norway rats. *Exp Eye Res*. 2005;80(6):877–884.

34. Lye-Barthel M, Sun D, Jakobs TC. Morphology of astrocytes in a glaucomatous optic nerve. *Invest Ophthalmol Vis Sci*. 2013;54(2):909–917.

35. Liu B, Neufeld AH. Expression of nitric oxide synthase-2 (NOS-2) in reactive astrocytes of the human glaucomatous optic nerve head. *Glia*. 2000;30(2):178–186.

36. Koch SM, Ullian EM. Neuronal pentraxins mediate silent synapse conversion in the developing visual system. *J Neurosci*. 2010;30(15):5404–5414.

37. Howell GR, Macalinao DG, Sousa GL, et al. Molecular clustering identifies complement and endothelin induction as early events in a mouse model of glaucoma. *J Clin Invest*. 2011;121(4):1429–1444.

38. Howell GR, MacNicoll KH, Braine CE, et al. Combinatorial targeting of early pathways profoundly inhibits neurodegeneration in a mouse model of glaucoma. *Neurobiol Dis*. 2014;71:44–52.

39. Williams PA, Braine CE, Kizhatil K, et al. Inhibition of monocyte-like cell extravasation protects from neurodegeneration in DBA/2J glaucoma. *Mol Neurodegener*. 2019;14(1):6.

40. Chung HS, Harris A, Kagemann L, Martin B. Peripapillary retinal blood flow in normal tension glaucoma. *Br J Ophthalmol*. 1999;83(4):466–469.

41. Weber AJ, Zelenak D. Experimental glaucoma in the primate induced by latex microspheres. *J Neurosci Methods*. 2001;111(1):39–48.

42. Weinreb RN, Khaw PT. Primary open-angle glaucoma. *Lancet*. 2004;363(9422):1711–1720.

43. Büchi ER, Suivaizdis I, Fu J. Pressure-induced retinal ischemia in rats: an experimental model for quantitative study. *Ophthalmologica*. 1991;203(3):138–147.

44. Adachi M, Takahashi K, Nishikawa M, Miki H, Uyama M. High intraocular pressure-induced ischemia and reperfusion injury in the optic nerve and retina in rats. *Graefes Arch Clin Exp Ophthalmol*. 1996;234(7):445–451.

45. Takita H, Yoneya S, Gehlbach PL, Duh EJ, Wei LL, Mori K. Retinal neuroprotection against ischemic injury mediated by intraocular gene transfer of pigment epithelium-derived factor. *Invest Ophthalmol Vis Sci*. 2003;44(10):4497–4504.

46. Crowston JG, Kong YX, Trounce IA, et al. An acute intraocular pressure challenge to assess retinal ganglion cell injury and recovery in the mouse. *Exp Eye Res*. 2015;141:3–8.

47. Chidlow G, Wood JPM, Casson RJ. Investigations into hypoxia and oxidative stress at the optic nerve head in a rat model of glaucoma. *Front Neurosci*. 2017;11:478.

48. Foxton RH, Finkelstein A, Vijay S, et al. VEGF-A is necessary and sufficient for retinal neuroprotection in models of experimental glaucoma. *Am J Pathol*. 2013;182(4):1379–1390.

49. El-Danaf RN, Huberman AD. Characteristic patterns of dendritic remodeling in early-stage glaucoma: evidence from genetically identified retinal ganglion cell types. *J Neurosci*. 2015;35(6):2329–2343.

50. Crish SD, Sappington RM, Inman DM, Horner PJ, Calkins DJ. Distal axonopathy with structural persistence in glaucomatous neurodegeneration. *Proc Natl Acad Sci USA*. 2010;107(11):5196–5201.

51. Chidlow G, Ebneter A, Wood JPM, Casson RJ. The optic nerve head is the site of axonal transport disruption, axonal cytoskeleton damage and putative axonal regeneration failure in a rat model of glaucoma. *Acta Neuropathol*. 2011;121(6):737–751.

52. Pease ME, McKinnon SJ, Quigley HA, Kerrigan-Baumrind LA, Zack DJ. Obstructed axonal transport of BDNF and its receptor TrkB in experimental glaucoma. *Invest Ophthalmol Vis Sci*. 2000;41(3):764–774.

53. Quigley HA, McKinnon SJ, Zack DJ, et al. Retrograde axonal transport of BDNF in retinal ganglion cells is blocked by acute IOP elevation in rats. *Invest Ophthalmol Vis Sci*. 2000;41(11):3460–3466.

54. Sossi N, Anderson DR. Blockage of axonal transport in optic nerve induced by elevation of intraocular pressure. Effect of arterial hypertension induced by angiotensin I. *Arch Ophthalmol*. 1983;101(1):94–97.

55. Johansson JO. Inhibition and recovery of retrograde axoplasmic transport in rat optic nerve during and after elevated IOP in vivo. *Exp Eye Res*. 1988;46(2):223–227.

56. Abbott CJ, Choe TE, Lusardi TA, Burgoyne CF, Wang L, Fortune B. Evaluation of retinal nerve fiber layer thickness and axonal transport 1 and 2 weeks after 8 hours of acute intraocular pressure elevation in rats. *Invest Ophthalmol Vis Sci*. 2014;55(2):674–687.

57. Williams PA, Howell GR, Barbay JM, et al. Retinal ganglion cell dendritic atrophy in DBA/2J glaucoma. *PLoS One*. 2013;8(8):e72282.

58. Weber AJ, Chen H, Hubbard WC, Kaufman PL. Experimental glaucoma and cell size, density, and number in the primate lateral geniculate nucleus. *Invest Ophthalmol Vis Sci*. 2000;41(6):1370–1379.

59. Quigley HA, Addicks EM, Green WR. Optic-nerve damage in human glaucoma. 3. Quantitative correlation of nerve-fiber loss and visual-field defect in glaucoma, ischemic neuropathy, papilledema, and toxic neuropathy. *Arch Ophthalmol*. 1982;100(1):135–146.

60. De Leon JM, Cheung CY, Wong TY, et al. Retinal vascular caliber between eyes with asymmetric glaucoma. *Graefes Arch Clin Exp Ophthalmol*. 2015;253(4):583–589.

61. Amerasinghe N, Aung T, Cheung N, et al. Evidence of retinal vascular narrowing in glaucomatous eyes in an Asian population. *Invest Ophthalmol Vis Sci*. 2008;49(12):5397–5402.

62. Ciancaglini M, Guerra G, Agnifili L, et al. Fractal dimension as a new tool to analyze optic nerve head vasculature in primary open angle glaucoma. *In Vivo*. 2015;29(2):273–279.

63. Krishnamoorthy RR, Rao VR, Dauphin R, Prasanna G, Johnson C, Yorio T. Role of the ETB receptor in retinal ganglion cell death in glaucoma. *Can J Physiol Pharmacol*. 2008;86(6):380–393.

64. Gericke A, Mann C, Zadeh JK, et al. Elevated intraocular pressure causes abnormal reactivity of mouse retinal arterioles. *Oxid Med Cell Longev*. 2019;2019:9736047.

65. Terraciano AJ, Sidoti PA. Management of refractory glaucoma in childhood. *Curr Opin Ophthalmol*. 2002;13(2):97–102.

66. Stowell C, Burgoyne CF, Tamm ER, Ethier CR, Lasker/IRRF Initiative on Astrocytes and Glaucomatous Neurodegeneration Participants. Biomechanical aspects of axonal damage in glaucoma: a brief review. *Exp Eye Res*. 2017;157:13–19.